Plasmonic Metasurface for Directional and Frequency-Selective Thermal Emission

D. Costantini,[1,*] A. Lefebvre,[2] A.-L. Coutrot,[1] I. Moldovan-Doyen,[1] J.-P. Hugonin,[1] S. Boutami,[2] F. Marquier,[1] H. Benisty,[1] and J.-J. Greffet[1,†]

[1]*Laboratoire Charles Fabry, Institut d'Optique, CNRS, Université Paris-Sud, 2 avenue Augustin Fresnel, 91127 Palaiseau cedex, France*

[2]*Université Grenoble Alpes F-38000 Grenoble, France CEA, LETI, MINATEC Campus, F-38054 Grenoble, France*

(Received 5 November 2014; revised manuscript received 20 March 2015; published 30 July 2015)

Incandescent filaments and membranes are often used as infrared sources despite their low efficiency, broad angular emission, and lack of spectral selectivity. Here, we introduce a metasurface to control simultaneously the spectrum and the directivity of blackbody radiation. The plasmonic metasurface operates reliably at 600 °C with an emissivity higher than 0.85 in a narrow frequency band and in a narrow solid angle. This emitter paves the way for the development of compact, efficient, and cheap IR sources and gas detection systems.

DOI: 10.1103/PhysRevApplied.4.014023

I. INTRODUCTION

Electromagnetic radiation in the midinfrared (mid IR) spectral range provides useful information for matter analysis. The infrared absorption spectrum contains "fingerprints" of the most common molecular bonds, key to sample composition analysis. As a result, there is a strong demand for efficient and cheap light sources operating at room temperature (RT). Simple semiconductor structures such as light-emitting diodes (LED) based on interband transitions have a very low efficiency in the mid IR (namely, $\lambda > 3\ \mu$m). Since the radiative decay time of the electron is proportional to λ^3 and becomes longer than nonradiative decay times, nonradiative processes become predominant when λ increases and the LED radiative efficiency decreases accordingly. On the other hand, more sophisticated semiconductor devices, such as quantum cascade lasers (QCLs) based on intersubband transitions, are powerful sources that operate at RT for wavelengths $3\ \mu\text{m} < \lambda < 25\ \mu$m [1]. However, QCLs are fabricated with an epitaxial growth technique that is very expensive. In this landscape, incandescent sources are still the best candidate, surely in terms of cost, but also in regards to the absolute power whenever broad spectral features are considered (say, $\Delta\lambda/\lambda > 1\%$).

The simplest available incandescent sources are either globar or hot membranes. They are cheap but suffer from a number of limitations that have hampered their deployment. Their emitted radiation is quasi-isotropic and broadband. Hence, most of the emitted radiation is useless. From the point of view of efficiency, most of the heating energy goes into convection or conduction losses and unwanted radiation, leading to wall-plug efficiencies typically on the order of a few percent for lighting applications but as low as 10^{-4} for spectroscopic applications where the useful bandwidth is on the order of 100 nm and the operating temperature on the order of 1000 K. Low efficiencies are due to heat leakage through conduction, convection, and radiation into unwanted frequencies and directions. Since convection can be suppressed by operating under vacuum and conduction can be suppressed by a proper design as recently proposed [2], it appears that the ultimate efficiency limit for incandescent sources is due to emission into unwanted frequencies and directions. The upper bound of the efficiency is given by the radiative efficiency which we define as the ratio of the power emitted in the useful spectral and directional window divided by the total power emitted by the source. In other words, there is no fundamental limit preventing incandescent sources from reaching 100% efficiency of incandescent sources. It is, thus, of critical importance to develop novel sources allowing the simultaneous control of the emission spectrum and the angular emission pattern so as to suppress unwanted radiation. In this paper, we introduce a metasurface that has a peak emissivity of 95% in the normal direction at 4.25 μm corresponding to a CO_2 absorption line. It emits in a limited solid angle (0.84 sr) and in a frequency interval with a full width at half maximum (FWHM) of 200 nm. Its radiative efficiency is 3.1%. This is to be compared with the theoretical radiative efficiency of a blackbody membrane, which is 0.5%, as implemented in state-of-the-art sources [3,4]. Furthermore, it can be operated at 650 °C in ambient conditions reliably.

The emitted power at a given frequency ω, direction $\mathbf{u}$, and temperature T is characterized by the emissivity $\varepsilon(\omega, \mathbf{u})$ defined by $L(\omega, \mathbf{u}, T) = \varepsilon(\omega, \mathbf{u}) L_{\text{BB}}(\omega, T)$ where

*Present address: Saint Gobain Recherche, 39 quai L. Lefranc, 93303 Aubervilliers Cedex, France.

†jean-jacques.greffet@institutoptique.fr

$L(\omega, \mathbf{u}, T)$ is the spectral radiance of the structure [5], and $L_{BB}(\omega, T)$ is the spectral radiance of the blackbody. The emissivity depends on the emission direction as well as on the frequency and acts as a filter of the blackbody spectral radiance to shape the emitted radiation from the thermal source. The polarization dependence is also included in the emissivity. In what follows, we consider only the averaged emissivity over the two polarizations $\varepsilon = (\varepsilon_s + \varepsilon_p)/2$. According to Kirchhoff's law, the emissivity ε is equal to the absorption α [5], reducing the problem of the ε calculation to a study of the reflectivity R for an opaque medium. Indeed, energy conservation for an incident beam yields $\alpha = 1 - R$. For a periodic metasurface of period p, the reflectivity is the sum of the power reflected in all propagating orders in both polarizations s and p: $R = \sum_{n,m}(R^s_{nm} + R^p_{nm})$, namely, the orders n, m such that the z wave vector component in vacuum $\gamma_{nm} = \{(4\pi^2/\lambda^2) - [K_x + n(2\pi/P)]^2 - [K_y + m(2\pi/P)]^2\}^{1/2}$ is a real number with K_x and K_y the in-plane projections of the vector $(\omega/c)\mathbf{u}$, c being the speed of light.

Many different approaches have been reported to control the emission spectrum of surfaces [6–21]. A review can be found in Ref. [22]. These incandescent sources are quasi-isotropic sources (spatially incoherent) as opposed to antennas or lasers which produce directional beams (spatially coherent). Yet, highly directional incandescent sources have been demonstrated in the last ten years [23–27]. Despite a large number of contributions regarding either spectrally selective or directional thermal sources, to the best of our knowledge, there is only one report of a thermal source that combines both properties. By inserting 63 quantum wells in an otherwise transparent semiconductor, a narrow spectrum absorber has been realized [28]. In addition, by patterning the material with a photonic-crystal structure, it is possible to control the angular pattern of emission. This realization is, however, nearly as demanding technologically as QCLs. From the data published in Ref. [28], we estimate the radiative efficiency (i.e., the power emitted in the spectral window and the solid angle normalized by the electrical power used to heat the source) to be 0.45%.

II. DIRECTIONAL AND SPECTRALLY SELECTIVE PLASMONIC METASURFACE

In this work, we use a plasmonic metasurface for the design and fabrication of an incandescent source which is both spectrally selective, directional, and fairly simple. Metasurfaces have been introduced in the last ten years for a number of applications [29–35]. Here, we use a 2D periodic array of metal-insulator-metal (MIM) cavities. Each MIM supports a gap surface plasmon (GSP) mode responsible for the resonant absorption or emission. Because of the subwavelength size of the cavity, the GSP resonance of a single antenna is obviously isotropic, which means that no directivity can be obtained. We show

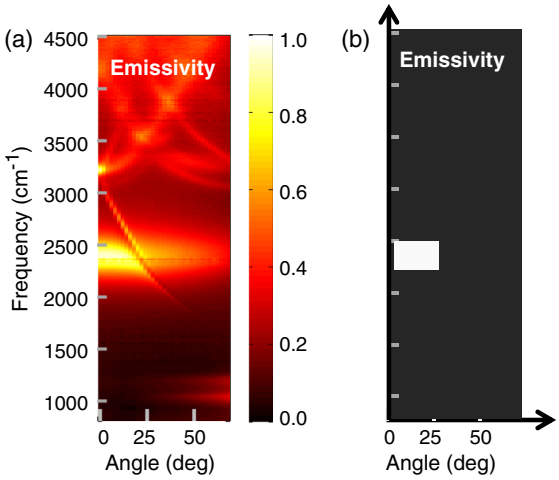

FIG. 1 (a) Direct measurement of the emissivity at 600 °C as a function of the frequency and the angle of the metasurface reported in this paper (W/SiN/Pt). The emissivity peak is located at $\omega = 2353$ cm^{-1} ($\lambda = 4.25$ μm) and between 0° and 26°. The complete characterization of the structure is shown in Fig. 5. (b) Schematics of the ideal source in the frequency angle plane. The emissivity should be 1 in the useful window and 0 elsewhere.

that while the individual MIM geometry allows the control of the resonance frequency, the directivity of the emitted radiation is, nonetheless, driven by the periodicity of the MIM array. We introduce a design procedure that allows us to vary the solid angle and the operating frequency by changing the metasurface parameters with great flexibility. The central result of this paper is the experimental measurement of the metasurface emissivity shown in Fig. 1. It takes significant values in a narrow frequency interval centered at $\omega = 2353$ cm^{-1} ($\lambda = 4.25$ μm, relative FWHM of approximately 16%) and for angles $\theta < 30°$, in a solid angle 0.84 sr. The choice of materials (W/SiN/Pt) borrowed from Refs. [3,4] is MEMS compatible and high-temperature compatible.

III. METASURFACE DESIGN AND FABRICATION

The metasurface is composed of a metal backplane, a continuous silicon nitride (SiN) insulator layer of height h_{SiN}, and a 2D periodic square array (period p) of metal squares of height $h_{metal} = 100$ nm and side L. Since the backplane is much thicker ($h_{backplane} = 200$ nm) than the mid IR metal skin depth, it is opaque. The actual substrate (i.e., silicon) is not playing any role in the device emissivity. We choose a geometry in which the GSP mode is confined along surface directions thanks only to the discontinuity induced by the metal patch edges (the insulator film is continuous [34]) and well depicted by the associated GSP lateral reflection factor. In order to explain the metasurface properties we will, from now on, show the numerical and experimental results obtained with a structure made of

Au/SiN/Au (backplane, spacer, and patches, respectively). Au is chosen as a model material to demonstrate the electromagnetic proof of concept but cannot be used to operate reliably at high temperature and is not complementary metal-oxide-semiconductor (CMOS) compatible. In the last part of the paper, we report the results obtained with a structure made of W/SiN/Pt. These materials can be used up to 900 K. Note that the SiN layer prevents the oxidation of the tungsten backplane.

Once the materials are chosen, the frequency and the intensity of the GSP resonance merely depend on the geometrical parameters h_{SiN} and L. We first engineer the MIM cavity to tune the resonance with the CO_2 absorption line in the range $2353 \pm 60\ \mathrm{cm}^{-1}$ using a refractive index of 1.77 for the SiN and Palik's data [36] for Au. We perform a numerical calculation with the rigorous coupled-waves analysis (RCWA) method in order to calculate and optimize the absorption at $\omega = 2353\ \mathrm{cm}^{-1}$, with a fixed period ($p = 3\ \mu$m), as a function of the spacer height h_{SiN} and the patch side L. The result in Fig. 2 shows an absorptivity $\alpha > 99\%$ for the operating point $h_{SiN} = 120$ nm and $L = 0.9\ \mu$m $(= 0.3p)$. We also observe that the absorptivity remains close to unity for the height range $h_{SiN} = 120 \pm 20$ nm, a large tolerance interval exceeding that of common SiN deposition techniques. The inset of Fig. 2 shows the section of the MIM cavity along the Oxz symmetry plane. The plotted absolute value of the total electric field for the chosen optimal case of $h_{SiN} = 120$ nm and $L = 0.9\ \mu$m exhibits a strong confinement in the SiN.

After defining the MIM size and height, we perform an absorptivity calculation of the structure as a function of the frequency and the parallel component of the wave vector

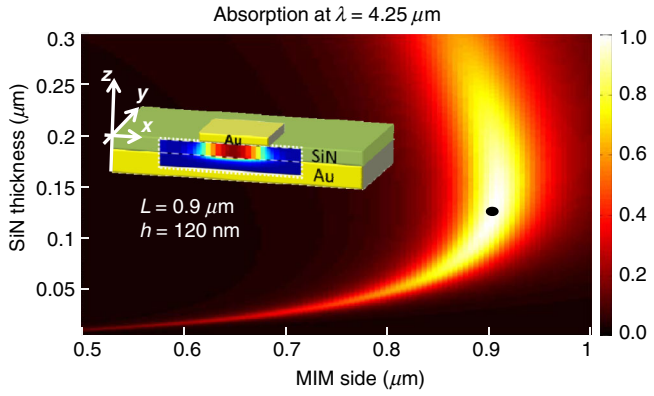

FIG. 2 Calculated absorption at normal incidence obtained with RCWA of a 2D MIM square grating (period of 3 μm) as a function of the SiN thickness and of the MIM side. The calculation is performed on the Au/SiN/Au structure (see inset with the electric-field absolute value map at a cross section; minimum is blue, maximum is red) under normal incidence at $\lambda = 4.25\ \mu$m and provides, at this specific wavelength, the geometrical parameters ensuring maximum MIM absorption (critical coupling conditions). The 100% absorption takes place for $L = 900$ nm and $h_{SiN} = 120$ nm (black dot).

$(K = K_x)$. The calculation result shown in Fig. 3(a) clearly displays a MIM resonance at $\omega = 2353\ \mathrm{cm}^{-1}$, visible for all the K range and standing out against the low background (equivalent to no absorption). The grating periodicity introduces obviously diffracted orders. As a result, on Fig. 3(a), an oblique line $\omega = 2\pi c/p - cK$ cuts the MIM horizontal resonance line in two parts. On the left part (smaller values of K), only one propagating order exists, and the absorption is maximum. For larger K, a -1 diffracted order appears, and this new channel for scattering is the reason why the absorptivity decreases as discussed below. In other words, by controlling the period p, we can

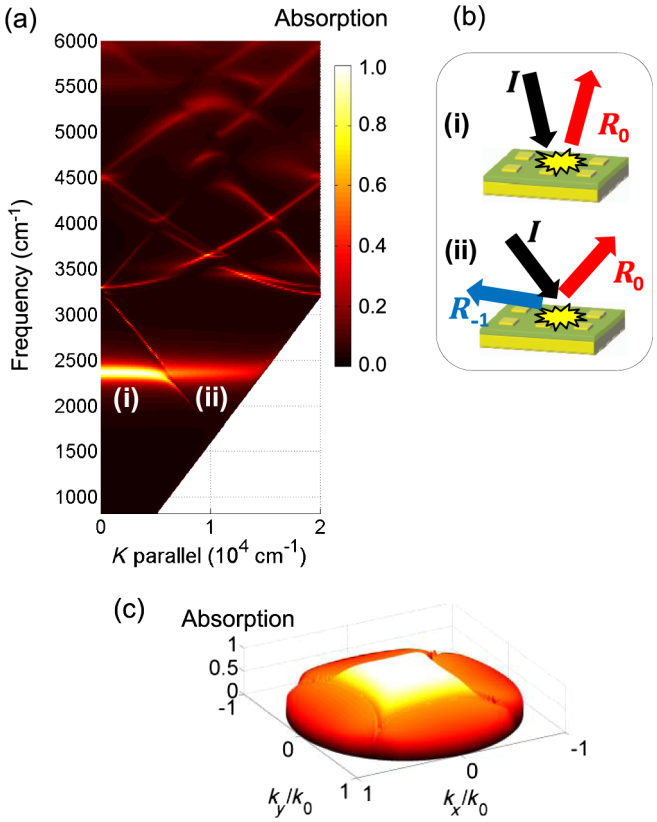

FIG. 3 (a) Calculated absorptivity as a function of the frequency and the incident K. The absorptivity is averaged over the two polarizations. The parameters of the simulated structure are $L = 900$ nm, $h_{SiN} = 120$ nm, and $p = 3\ \mu$m. The MIM resonance displays an absorption peak at $\omega = 2353\ \mathrm{cm}^{-1}$ $(\lambda = 4.25\ \mu\mathrm{m})$ for all incident wave vectors (angles). The oblique line $\omega = 2\pi c/p - cK$ (c being the speed of light) cuts the horizontal resonance line in two parts, with large absorption on the side of smaller K. (b) Schematics to explain the reduction of the absorption for large K: (i) for small K values, there is a single diffracted order, whereas (ii) for larger K values, there are two diffracted orders. The existence of the -1 order introduces an additional radiative decay channel so that the critical coupling condition is no longer fulfilled. (c) Calculated absorptivity at $\lambda = 4.25\ \mu$m as a function of the normalized k_x and k_y. It is clearly seen that the presence of the grating allows controlling of the directivity of the absorption and emission.

design the angular width of the emitter. More precisely, the position of this first-order cutoff is given by $\sin^{-1}[(\lambda - p)/p]$. Here, with $p = 3$ μm and $\lambda = 4.25$ μm, we find $\theta = 24.6°$.

IV. PHYSICAL MECHANISM FOR DIRECTIONALITY

The physical mechanism responsible for the absorptivity control can be understood as follows: The total absorption is due to a critical coupling to the GSP resonator [15] at normal incidence in a regime having a single (specular) diffracted order; Fig. 3(b) panel (i). When a second nonspecular order is allowed [Fig. 3(b) panel (ii)], radiative losses are modified (basically, they are increased) so that the critical coupling condition is no longer fulfilled. It follows that the absorption is reduced. We explore the absorption for different azimuthal angles by solving the full 3D problem. We plot in Fig. 3(c) the polarization-averaged absorptivity $(\alpha_s + \alpha_p)/2$ as a function of the emission direction at $\omega = 2353$ cm^{-1}. We observe a large absorption in a square-bounded (pyramidlike) solid angle rather than a cone of cylindrical symmetry, with a minimum apex semiangle of 26° along the x axis. The subtended square-shaped solid angle is larger by a factor of only approximately $4/\pi$ than that of the inscribed cone, not a crucial change of directivity for most instrumental optics. In summary, tuning the parameters of a periodic array of gap-plasmon patch resonators provides enough room for designing a metasurface with an emissivity close to unity in a controlled spectral bandwidth *and* in a controlled solid angle.

V. FABRICATION AND ROOM-TEMPERATURE CHARACTERIZATION

The device simulated above based on Au cavities with $h_{\mathrm{SiN}} = 120$ nm, $L = 920$ nm, and $p = 3$ μm is fabricated and experimentally measured; see Fig. 4(a). The Au backplane of thickness 200 nm is evaporated on a Si wafer after deposition of a 10-nm-thick Ti adhesion layer. SiN is deposited by plasma-enhanced chemical-vapor deposition. The square patches are defined by electron-beam lithography with a lift-off process using the evaporation of a 100-nm-thick gold layer again onto a 3-nm-thick Ti adhesion layer. Unlike the first gold adhesion layer, this thin Ti layer has to be as thin as possible in order to avoid broadening the resonance. A micrograph of the sample is presented in Fig. 4(a) with typical values of the patch side and period.

We measure first the room-temperature specular reflectance of this device. Measurements are performed with a Vertex 70 Bruker Fourier-transform infrared spectrometer (FTIR) using a reflectivity module. We use the internal MIR light source, the KBr beam splitter, and a liquid-nitrogen-cooled mercury-cadmium-telluride detector. The result of the measurement is shown in Fig. 4(b) by mapping $1 - R_0$,

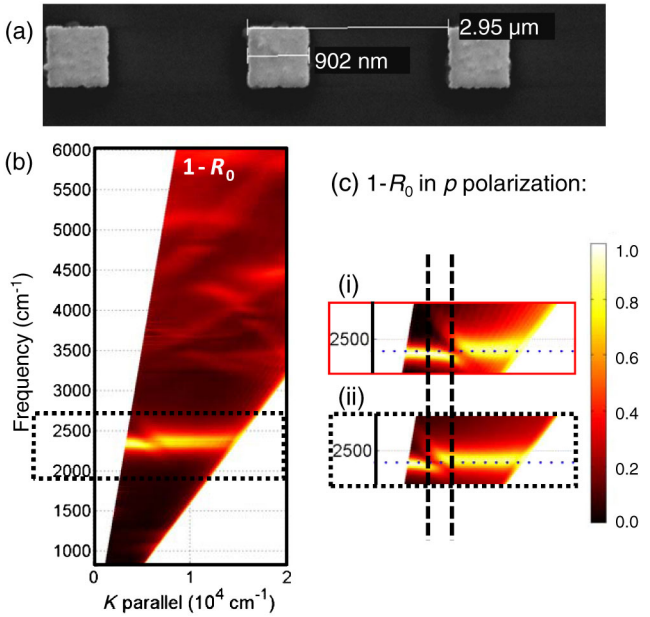

FIG. 4 (a) SEM image of the MIM grating showing the size of the square side and of the period. (b) Measured reflectivity R_0 normalized by a gold surface, plotted as the map of $1 - R_0$. The experimental measurement spans from 13° to 90° and allows observation of the anticrossing point due to strong coupling between the MIM resonance and the plasmon. On the left side (smaller K) of this crossing line, the quantity $1 - R_0$ equals the absorption, and the figure can be compared to Fig. 3(a). (c) Enlarged anticrossing zone in the measured $1 - R_0$ map in p polarization for samples with $L = 900$ nm and different periods, (i) $p = 2.7$ μm, (ii) $p = 3$ μm. By decreasing the period, the anticrossing point shifts towards higher K (vertical dashed line).

where R_0 is the measured (specular) reflectance in the zeroth order. When only the specular (zeroth) order exists, in the central part of the Brillouin zone (smaller K), the quantity $1 - R_0$ corresponds to the absorption, and Fig. 4(b) can be directly compared to Fig. 3(a). In this region, R_0 is close to 0 so that the absorption is maximum, as predicted in the calculations. When K becomes larger, the diffracted order -1 becomes propagating, and the absorption becomes $1 - R_0 - R_{-1}$ so that $1 - R_0$ is no longer the absorptivity. To better appreciate the degree of control on the source directivity, we report in Fig. 4(c) two reflection factor measurements for two different periods differing by 10%, $p = 3$ μm, $p = 2.7$ μm, and for p polarization only. It can be observed that, as predicted, the period does not affect the frequency of the MIM resonance but unambiguously shifts the crossing point indicated by dashed lines.

VI. HIGH-TEMPERATURE EMITTER USING TUNGSTEN

To perform emission measurements at high temperature, we fabricate a W/SiN/Pt sample with a tungsten (W) backplane, a SiN insulator layer, and sturdy platinum (Pt)

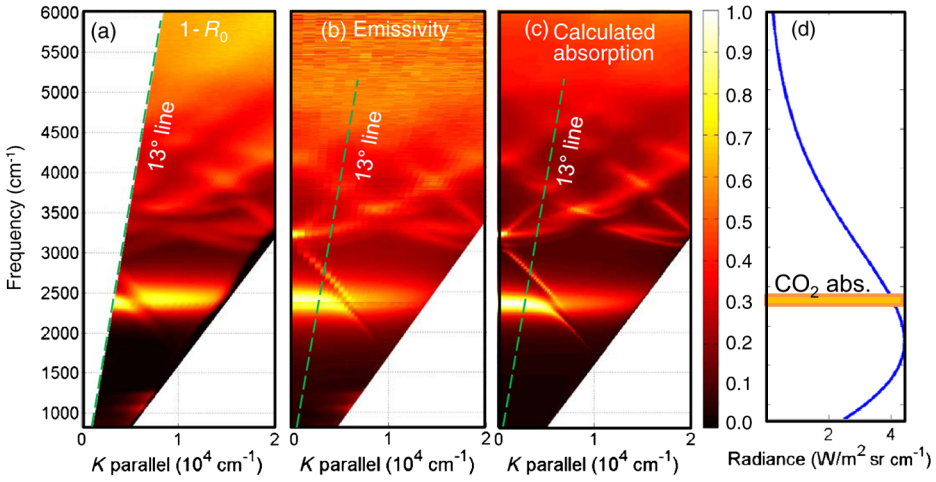

FIG. 5 Characterization of the W/SiN/Pt metasurface, with height $h_{SiN} = 210$ nm and patch side $L = 855$ nm, as a function of the frequency and wave vector K. (a) Measured map of $1 - R_0$ normalized by a gold surface (from 13° to 90°). (b) Measured emissivity at 600 °C obtained by normalizing with a blackbody reference (from 0° to 70° angles, with the 13° line as a guide to the eye). (c) Calculated absorption for a direct comparison with the emissivity. (d) The calculated blackbody radiance at 600 °C with the frequency interval of the CO_2 absorption (from 4.16 to 4.36 μm).

square patches. Using the Palik [34] refractive indices for W and Pt, we numerically optimize the MIM cavity parameters obtaining $h_{SiN} = 210$ nm and $L = 855$ nm, the largest change being the larger height. The fabrication process is the same as described above except that W and Pt are deposited by sputtering. The emissivity measurement is performed by heating the sample at 600 °C (873 K) on a holder, which is fixed on a motorized rotating goniometer. The emitted thermal radiation is collected with a mirror system and sent into the Bruker FTIR spectrometer [24]. By replacing the sample with a calibrated blackbody (SR 200 ECI system), we get an adequate reference in order to fully determine the emissivity. This setup provides us with a direct measurement of the emissivity $\varepsilon(\omega, \mathbf{u})$ with an angular resolution of 0.5°.

The sample characterization through its reflectivity is shown in Fig. 5(a). It is quite similar to the previous sample, with only a slightly broader absorption band, as expected. The experimental emissivity map is shown in Fig. 5(b) and is in very good agreement with the map predicted by the numerical calculation, Fig. 5(c). The 13° limit is indicated for comparison to Fig. 5(a). The decrease of emissivity for large K, which cannot be inferred from specular reflection measurement on Fig. 5(a), appears clearly now. The resonance peak culminates at 95% at $\omega = 2390$ cm^{-1} and has a FWHM of 370 cm^{-1}, whereas the numerical calculation gives a peak of 100% at 2350 cm^{-1} with a FWHM of 250 cm^{-1}. We attribute the peak broadening at high temperature to a thermal evolution of the refractive indices. The rightmost panel of Fig. 5 shows the theoretical radiance of a blackbody at 600 °C highlighting the useful frequency interval for CO_2 detection and its proximity to the Wien wavelength in that case.

VII. FIGURE OF MERIT FOR CO_2 SPECTROSCOPY AND CONCLUSION

To quantify the gain with respect to the blackbody, we define a *useful spectral window* ($\omega = 2353 \pm 60$ cm^{-1}), which corresponds to the CO_2 absorption band, while for the solid angle, we take into account a cone with a semiangle of 25°. Using the data of Fig. 5(b) at normal incidence, we find that the device emits 85% of the power of a blackbody in the *useful spectral window*. Hence, the device is almost nearly as good as a blackbody for the desired radiation. We now examine the radiative efficiency that we defined as the total power emitted in the useful spectral and spatial window divided by the total power emitted by the source. This figure of merit is 0.5% for a blackbody membrane given the small cone and reaches experimentally a 6 times higher value of 3.1% for the engineered metasurface.

In summary, we experimentally demonstrate a metasurface for directional and frequency-selective thermal emission designed for operation at 600 °C. We suggest a practical application as a source for CO_2 detection showing radiative performances equivalent to a blackbody but with a radiative efficiency enhanced by a factor of 6.2. The emission of the metasurface can be easily tuned with geometrical parameters well within process and lithographic capabilities. The concept can be adapted to multichannel emission using various MIM cavities of different sizes. All the technology is CMOS compatible allowing integration in cheap wafer-scale industrially processed sources. This type of design can also be implemented for thermophotovoltaic applications.

ACKNOWLEDGMENTS

This work is supported by the French National Research Agency (Project No. ANR-12-NANO-0005 "IDEE"). We thank P. Barritault for useful discussions. We thank M. Besbes for the help in finite element simulations and D. Daineka for the support in fabrication. The device fabrication has been performed in the Thales and IOGS facilities.

[1] Y. Yao, A. J. Hoffman, and C. Gmachl, Mid-infrared quantum cascade lasers, Nat. Photonics **6**, 432 (2012).

[2] G. Brucoli, P. Bouchon, R. Haidar, M. Besbes, H. Benisty, and J.-J. Greffet, High efficiency quasi-monochromatic infrared emitter, Appl. Phys. Lett. **104**, 081101 (2014).
[3] P. Barritault, M. Brun, S. Gidon, and S. Nicoletti, Mid-IR source based on a free-standing microhotplate for autonomous CO_2 sensing in indoor applications, Sens. Actuators A Phys. **172**, 379 (2011).
[4] P. Barritault, M. Brun, O. Lartigue, J. Willemin, J.-L. Ouvrir-Buffet, S. Pocas, and S. Nicoletti, Low power CO_2 NDIR sensing using a micro-bolometer detector and a micro-hotplate IR-source, Sens. Actuators B Chem. **182**, 565 (2013).
[5] J.-J. Greffet and M. Nieto-Vesperinas, Field theory for generalized bidirectional reflectivity: Derivation of Helmholtz's reciprocity principle and Kirchhoff's law, J. Opt. Soc. Am. A **15**, 2735 (1998).
[6] P. Hesketh, J. Zemel, and B. Gebhart, Organ pipe radiant modes of periodic micromachined silicon surfaces, Nature (London) **324**, 549 (1986).
[7] G. N. Zhizhin, E. A. Vinogradov, M. A. Moskalova, and V. A. Yakovlev, Applications of surface polaritons for vibrational spectroscopic studies of thin and very thin films, Appl. Spectrosc. Rev. **18**, 171 (1982).
[8] E. Rephaeli and S. Fan, Absorber and emitter for solar thermo-photovoltaic systems to achieve efficiency exceeding the Shockley-Queisser limit, Opt. Express **17**, 15145 (2009).
[9] O. G. Kollyukh, A. I. Liptuga, V. Morozhenko, and V. I. Pipa, Thermal radiation of plane-parallel semitransparent layers, Opt. Commun. **225**, 349 (2003).
[10] J. Drevillon and P. Ben-Abdallah, *Ab initio* design of coherent thermal sources, J. Appl. Phys. **102**, 114305 (2007).
[11] B. J. Lee and Z. M. Zhang, Design and fabrication of planar multilayer structures with coherent thermal emission characteristics, J. Appl. Phys. **100**, 063529 (2006).
[12] A. Battula and S. C. Chen, Monochromatic polarized coherent emitter enhanced by surface plasmons and a cavity resonance, Phys. Rev. B **74**, 245407 (2006).
[13] I. Celanovic, D. Perreault, and J. Kassakian, Resonant-cavity enhanced thermal emission, Phys. Rev. B **72**, 075127 (2005).
[14] I. Puscasu and W. L. Schaich, Narrow-band, tunable infrared emissions from arrays of microstrip patches, Appl. Phys. Lett. **92**, 233102 (2008).
[15] B. J. Lee, L. P. Wang, and Z. M. Zhang, Coherent thermal emission by excitation of magnetic polaritons between periodic strips and a metallic film, Opt. Express **16**, 11328 (2008).
[16] Y. Avitzour, Y. A. Urzhumov, and G. Shvets, Wide-angle infrared absorber based on a negative-index plasmonic metamaterial, Phys. Rev. B **79**, 045131 (2009).
[17] C. M. Wang, Y. C. Chang, M. N. Abbas, M. H. Shih, and D. P. Tsai, T-shaped plasmonic arrays as a narrow-band thermal emitter or biosensor, Opt. Express **17**, 13526 (2009).
[18] N. Liu, M. Mesch, T. Weiss, M. Hentschel, and H. Giessen, Infrared perfect absorber and its application as plasmonic sensor, Nano Lett. **10**, 2342 (2010).
[19] X. Liu, T. Tyler, T. Starr, A. F. Starr, N. M. Jokerst, and W. J. Padilla, Taming the Blackbody with Infrared Metamaterials as Selective Thermal Emitters, Phys. Rev. Lett. **107**, 045901 (2011).
[20] P. Bouchon, C. Koechlin, F. Pardo, R. Haidar, and J.-L. Pelouard, Wideband omnidirectional infrared absorber with a patchwork of plasmonic nanoantennas, Opt. Lett. **37**, 1038 (2012).
[21] H. T. Miyazaki, T. Kasaya, M. Iwanaga, B. Choi, Y. Sugimoto, and K. Sakoda, Dual-band infrared metasurface thermal emitter for CO_2 sensing, Appl. Phys. Lett. **105**, 121107 (2014).
[22] C. Fu and Z. M. Zhang, Thermal radiative properties of metamaterials and other nanostructured materials: A review, Front. Energy Power Eng. China **3**, 11 (2009).
[23] J.-J. Greffet, R. Carminati, K. Joulain, J.-P. Mulet, S. Mainguy, and Y. Chen, Coherent emission of light by thermal sources, Nature (London) **416**, 61 (2002).
[24] M. Laroche, C. Arnold, F. Marquier, R. Carminati, J.-J. Greffet, S. Collin, N. Bardou, and J.-L. Pelouard, Highly directional radiation generated by a tungsten thermal source, Opt. Lett. **30**, 2623 (2005).
[25] N. Dahan, A. Niv, G. Biener, Y. Gorodetski, V. Kleiner, and E. Hasman, Enhanced coherency of thermal emission: Beyond the limitation imposed by delocalized surface waves, Phys. Rev. B **76**, 045427 (2007).
[26] C. Arnold, F. Marquier, M. Garin, F. Pardo, S. Collin, N. Bardou, J.-L. Pelouard, and J.-J. Greffet, Coherent thermal infrared emission by two-dimensional silicon carbide gratings, Phys. Rev. B **86**, 035316 (2012).
[27] S. Han and D. Norris, Beaming thermal emission from hot metallic bull's eyes, Opt. Express **18**, 4829 (2010).
[28] M. De Zoysa, T. Asano, K. Mochizuki, A. Oskooi, T. Inoue, and S. Noda, Conversion of broadband to narrowband thermal emission through energy recycling, Nat. Photonics **6**, 535 (2012).
[29] Z. Bomzon, G. Biener, V. Kleiner, and E. Hasman, Space-variant Pancharatnam-Berry phase optical elements with computer-generated subwavelength gratings, Opt. Lett. **27**, 1141 (2002).
[30] N. Yu, P. Genevet, M. A. Kats, F. Aieta, J.-P. Tetienne, F. Capasso, and Z. Gaburro, Light propagation with phase discontinuities: Generalized laws of reflection and refraction, Science **334**, 333 (2011).
[31] N. Yu, F. Aieta, P. Genevet, M. A. Kats, Z. Gaburro, and F. Capasso, A broadband, background-free quarter-wave plate based on plasmonic metasurfaces, Nano Lett. **12**, 6328 (2012).
[32] X. Ni, N. K. Emani, A. V. Kildishev, A. Boltasseva, and V. M. Shalaev, Science **335**, 427 (2012).
[33] F. Monticone, N. M. Estakhri, and A. Alù, Broadband Light Bending with Plasmonic Nanoantennas, Phys. Rev. Lett. **110**, 203903 (2013).
[34] A. Pors and S. I. Bozhevolnyi, Plasmonic metasurfaces for efficient phase control in reflection, Opt. Express **21**, 27438 (2013).
[35] A. V. Kildishev, A. Boltasseva, and V. M. Shalaev, Planar photonics with metasurfaces, Science **339**, 1232009 (2013).
[36] E. D. Palik, *Handbook of Optical Constants of Solids* (Academic Press, New York, 1985).